Characterising texture formation in fibre lattices embedded in a nematic liquid crystal matrix

P. M. PHILLIPS and A. D. REY

Department of Chemical Engineering, McGill University, Montreal, Quebec, Canada H3A 2B2
e-mail: paul.phillips@mail.mcgill.ca

A two-dimensional computational study is performed on the texturing of fibre-filled nematic liquid crystals using the Landau-de Gennes model describing the spatio-temporal evolution of the second moment of the orientation distribution function or quadrupolar tensor order parameter. The investigation is performed on a consistent computational domain comprising a square array of four circular fibres embedded within a unit square containing a uniaxial low molar mass calamitic liquid crystal. Interest is focused on the role of temperature, boundary conditions and their effect on the nucleation and evolution of defect structures. Thermal effects are characterised below and above the temperature at which the nematic state is stable. Simulations in the stable nematic state serves as a scenario for investigating the effect of imposing different external boundary conditions, namely periodic and Dirichlet; the former describes a square lattice array of fibres embedded in a nematic liquid crystal, and the latterdescribes a four-fibre arrangement in an aligned nematic material. In each case, the influence of temperature is characterised, with defect structures forming and either remaining or splitting into lower strength defects. For fibre lattices, splitting transitions of defects at the centre of the domain occur at a critical temperature, but for the four-fibre arrangement, defect transitions occur continuously over a temperature range. The discontinuous defect splitting transition in fibre arrays occurs at lower temperatures than the continuous defect transformation in the four-fibre arrangement. At sufficiently low temperatures, the four-fibre arrangement and the fibre lattice give the same texture consisting of two disclination lines close to each fibre. The evolution of the texture with respect to temperature can be characterised as a change from single-fibre mode at low temperature to a collective mode with a centre-located heterogeneity at higher temperature. At higher temperatures, in the stable isotropic state, it is shown that surface-induced ordering arising from the fibre/liquid crystal interaction propagates into the bulk forming thin disclination lattices around the four-fibre configuration.

Key words: Liquid Crystals; Defects; Fibre Lattices

1 Introduction

Liquid crystals are functional and structural materials with uses ranging from optical devices to superstrong fibres. Nematic liquid crystals (NLCs) have orientational order and are visco-elastic anisotropic materials. Their elasticity arises from orientational gradients and the characteristic modulus is in the pN range, thus placing them in the family of soft

matter. Synthetic or natural liquid crystals can exhibit novel properties through blending or mixing second phases. Filled nematic liquid crystals (FNs) are one class of two-phase blends.

Filled nematics refer to the suspension of second phases such as fibres, particles, drops, bubbles, etc. in a nematic liquid crystalline matrix. These materials arise spontaneously through phase separation processes between a polymer melt and a nematic liquid crystal, through dispersion of the second phase [13] or through flow of the NLC into a bundle of aligned fibres [17]. The latter form the basis of carbon/carbon composites formed by injecting a carbonaceous discotic nematic mesophase into the fibre tow [13]. Since nematic liquid crystals display gradient orientation elasticity, the interaction between the filler and nematic matrix phases usually leads to texturing and defect nucleation. Filled nematics form novel colloids with distinctive self-assembly properties and are precursors to high-performance composites in which the mesophase matrix itself possesses orientational order. The interested reader is referred to [27] for a comprehensive overview of the capillary modelling science of nematic liquid crystals and their applications to the stability, structure and shape of films, membranes, fibres and drops. The fundamental physics as well as engineering applications of filled nematics (and other phases such as cholesterics and smectic) are a fascinating evolving field.

A fundamental feature of FNs is that for sufficiently strong interaction between the filler and the NLCs, orientational anchoring at the curved interface propagates into the bulk, usually creating frustration that leads to the nucleation of orientational defects, such as disclinations [28].

One technique for characterising orientational defects is to consider the partial molecular order with respect to the average molecular order or director, **n**. As any orientation of **n** is possible, this leads to the possibility of defects or spatial discontinuities in **n**. The director profile associated with a defect will depend on the imposition and nature of anchoring conditions imposed by fibres within the system, such as whether these conditions are normal or tangential to the fibre surface. Figure 1(a) shows a representative orientation visualisation of a four-fibre arrangement under normal (homeotropic) boundary conditions, where the central dot represents a disclination line of strength +1. Under tangential anchoring conditions, (not shown), the central defect has strength –1 instead of +1. Figures 1(b) and (c) shows schematics of director path lines around the integer strength disclinations that typically arise in the centre region of a fibre-filled nematic.

The emphasis of this paper is on identifying and characterising the texture structures observed in fibre-filled nematics, of relevance to carbon/carbon structural composites and other FNs for potential device applications. The order of NLC is described by the molecular order parameters and the average macroscopic orientation. Localised heterogeneities in the liquid crystalline order are related to the presence of defects. Defects are commonly observed in NLCs and have been studied extensively [1, 5, 9, 16–18, 20, 32]. Defect structures play an important role in such phenomena as response to external stresses and the nature and type of phase transitions. The presence of these defects and their evolution may be attributed to anchoring conditions, surface geometry and external fields. Defects are classified into singular or non-singular depending on whether their core retains the equilibrium nematic order or not. In non-singular defect lines, the director escapes into the third dimension, the molecular order remains unchanged and the defect
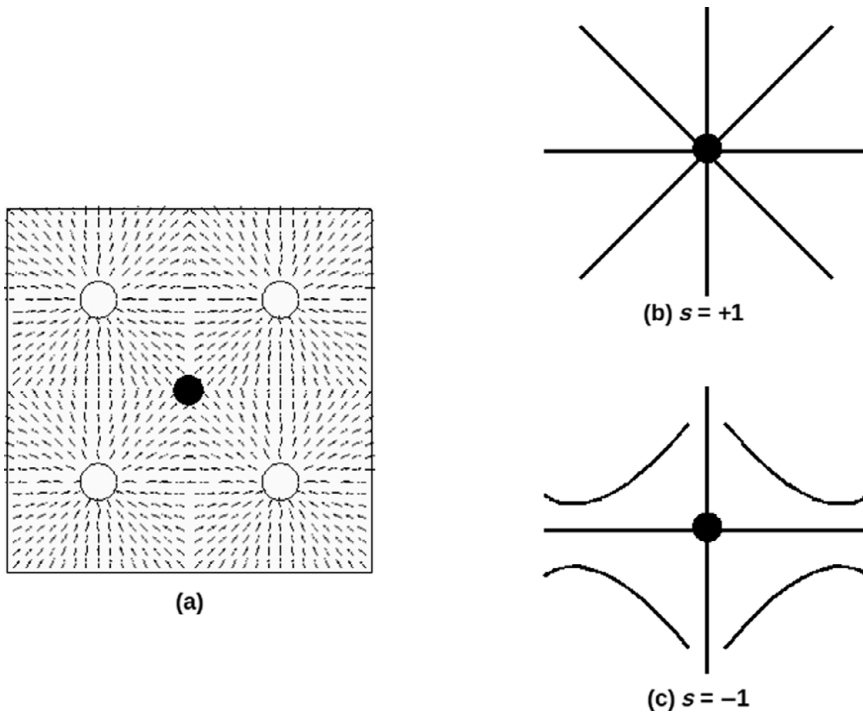
FIGURE 1. Examples of director (orientation) profiles in a fibre-filled nematic. The image in (a) is generated from a numerical solution where there is a disclination occurring in the centre, represented by the black dot; Dirichlet orientation conditions have been placed on the internal boundaries, normal to the surface. In the case of tangential Dirichlet orientation conditions, the centre region disclination would be of strength –1. The images, (b) and (c), are schematics representing director profiles associated with defects $s = +1$ and $s = -1$, respectively.

core size is in the micron range. In singular defect lines, the core is usually biaxial, and at the centreline, it is negatively uniaxial (as opposed to positively uniaxial in the equilibrium bulk state). Defects are classified in terms of strength, s, and dimensionality, D. The strength s of a defect refers to the number of rotations that the director experiences while encircling the defect, whereas the dimensionality refers to points, lines and inversion wall defects ($D = 0, D = 1, D = 2$), respectively. Point defects are usually disclination rings [8, 9]. Inversion wall defects are non-singular and describe localised continuous orientation gradients.

The literature on the forming of defect structures in liquid crystals from both computational and experimental discipline is wide and varied [3, 7, 19, 20]. For brevity, we concentrate on works of direct implication to texture the simulation of fibre-filled nematics on the basis of quadrupolar tensor order parameter models. Some of the earlier contributions were discussed by Zimmer and Weitz [32] which discuss both a computational and experimental study on the formation of defect structures in fibre lattices. More recently, the advancement of computational resources has allowed for an in-depth computational investigation. Fukuda and Yokoyama [11] have performed a very elegant numerical investigation into a liquid crystal nematic around a two-dimensional spherical

particle where an adaptive grid scheme is used to locally adjust with respect to the spatial gradient of the orientation parameter. They present computations where a hedgehog defect around the particle becomes unstable and splits from a -1 defect to 2 (-1/2) defects.

The interface plays a significant role in texturing in FNs, and new phenomena are expected with deformable inclusions. It is shown that the anisotropic elastic stress contribution to the surface stress tensor gives rise to bending stresses and tangential forces. When the tensor order parameter that predicts the NLC structure has surface gradients, a tensor order parameter-driven Marangoni flow is predicted. The strength of the predicted effect is proportional to the nematic–isotropic interaction energy characteristic of the interface, and the direction of flow is from low-energy regions towards high-energy regions. The role of convection on texturing in FNs remains poorly explored.

The work of Desmet *et al.* [22] has considered the liquid crystal director orientation in geometries with sharply defined edges and surfaces that impose strong anchoring and preferred direction. They have shown that the liquid crystal orientation behaviour close to an edge with planar anchoring may be approximated by a set of analytical formulas.

The work of Grecov and Rey [12] has provided results on numerical simulations on the Landau-de Gennes system which provide insight into textural transformations and dependence on temperature. The simulations have captured well-known and important nucleation processes such as defect–defect annihilation, defect pinching and defect escape. Grecov *et al.* [6] discuss other works on liquid crystal structuring and defect formation.

The works of Gupta *et al.* [14,17] have discussed the characterisation of defect structures in defect lattices further. In one case, [17], an integrated computational microstructural and optical model of disclination lattices in carbonaceous mesophase filled with small fibres has been developed, solved and validated from hydrodynamic structuring. The microstructural model that these authors have used has predicted the orientation and defect texture in the discotic nematic ordering of the carbonaceous mesophase. They have shown that the insertion of micron-sized particles on the mesophases creates a disclination network.

In the other case, [14], the defect textures in concentrated fibre-filled polygonal networks in nematic liquid crystals are analysed. The modelling is performed on the micron scale by using differential geometry and computational modelling based on the Landau-de Gennes theory. The topological rules of disclination strength have been established which state that for a polygonal network of N sides, the strength s is related as

$$s = \frac{(N-2)}{2}. \tag{1.1}$$

It is known that in such a system, the energy, E, of a defect is related to the disclination charge s by $E \propto s^2$. This explains the apparent defect splitting that is observed within these structures, as higher strength disclinations split into components of lower s and remain stable because of a lower energy state.

Temperature is known to affect disclination splitting under confinement. For example, in a capillary of radius R, defect splitting is given by

$$\frac{T}{T_u} = \frac{9}{8} - 3\left(\frac{R}{\epsilon} - C\right)^{-0.65}, \tag{1.2}$$

where T, T_u denote the temperature and the transition temperature for which the nematic phase is stable, respectively and ϵ denotes the correlation length (equation (2.16)). This function defines a curve on the texture phase diagram giving capillary radius as a function of temperature, such that above this curve a pure splay radial texture with a singular $+1$ disclination exists, while below a splay-bend texture with two $+1/2$ disclinations are found. Hence, the situation of sufficiently large capillary confinement approaching the nematic–isotropic transition temperature leads to the emergence of a single-singular defect with an expanded core. A similar trend is thus expected for the FN studied here with the difference that confinement is partial and complex.

With the advancement of computational resources in the last few years, we are able to extend texture simulation in fibre-filled nematics to a different length scale from Gupta *et al.* [14,17], and we consider our problem in the nanometre range. Wincure and Rey [36] have discussed the defect forming mechanism for liquid crystals undergoing an isotropic to nematic phase transition. Free energy density, defect core shapes and the evolving defect core structure are presented at the nanoscale to better understand liquid crystal anisotropy and orientation during interfacial defect spreading for a 5CB nanodroplet. We consider the spatio-temporal evolution of our defect structures as a function of temperature, characterising the regime transitions that exist. The influence of temperature regimes on texturing has been associated with the nematic–isotropic transition [18]. For the well-characterised compound 5CB [4], there are five important temperature ranges relating the temperature, T, to the stability criterion for the isotropic and nematic stages.

(1) $T < T^* = 307.2$: the isotropic phase is unstable, and the nematic phase is stable [4]. T^* is referred to as the spinodal temperature [24] or the supercooling limit.

(2) $T^* < T < T_c$: the isotropic phase is unstable and the nematic phase is stable. $T_c = 307.44$, is known as the critical temperature [24] or supercooling temperature.

(3) $T = T_c$: the free energy of the isotropic phase is equal to the free energy of the nematic phase.

(4) $T_c < T < T_u$: the isotropic phase is stable, and the nematic phase is metastable where T_u is known as the superheating limit, $T_u = 307.47$.

(5) $T < T_u$: the nematic phase is unstable, and the isotropic phase is stable.

The influence of temperature regimes on the formation of defect structures has been discussed by Mottram and Sluckin [21]. They have characterised the critical temperature required for the nucleation of defect structures. The behaviour of the core radius as a function of temperature has also been considered and compared with a previous numerical model of the effect [16].

As mentioned above, this paper considers a four-fibre square arrangement of an FN. In addition to temperature, this paper will also consider the influence of two characteristic types of external boundary conditions (Dirichlet and periodic) representing two different physical scenarios of a four-fibre square arrangement in an FN. Outer Dirichlet conditions represent four fibres embedded in an aligned nematic matrix. Outer periodic boundary conditions represent an infinite fibre lattice with square symmetry. Figure 2 shows the two FNs.
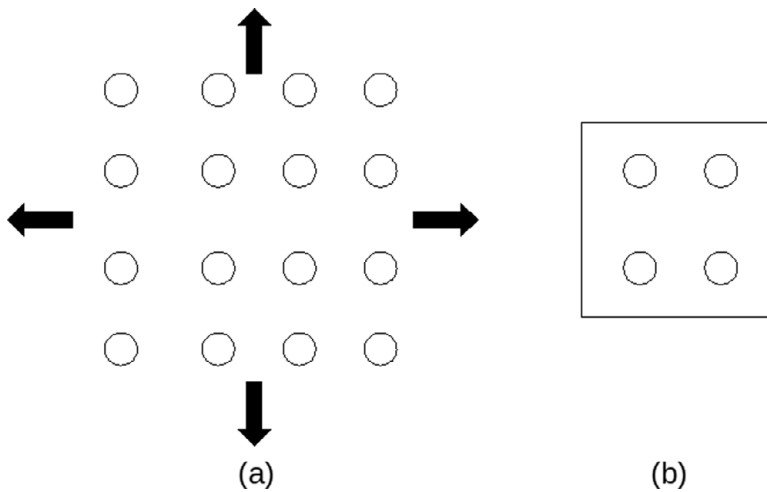
FIGURE 2. Schematic of the computational domain. The application of periodic external boundary conditions in (a) creates the effect of an infinite square lattice of fibres embedded in a nematic liquid crystal. The application of external Dirichlet boundary conditions in (b) creates the effect of a four-fibre arrangement in an aligned nematic material.

The boundary conditions in all internal boundaries are homeotropic, with the orientation radial to the circular fibre and with a level of molecular ordering dictated by temperature when the nematic phase is stable. When the isotropic state is stable, we also investigate the possible texturing effect that arises because of surface-induced ordering and long range order.

The specific objectives of this paper are as follows:

(1) To provide a brief introduction and history of the modelling of liquid crystal structures and current founded knowledge contributed by previous authors.

(2) To discuss our problem under investigation and the reason it is distinguished from previous work and provides a novel contribution to the area of liquid crystal modelling.

(3) To propose and solve a computational model for the evolution of defect structures in these systems.

(4) A discussion of our results and conclusions.

The present paper is restricted to two dimensions in physical space and five in phase space. The two-dimensional restrictions capture [14] the important features observed experimentally in carbonaceous mesophases filled with carbon fibres since the texture formation is a cross-sectional plane process. Likewise, two-dimensional texturing by carbonaceous mesophase flow through screens with square symmetry [17] is also efficiently characterised by a reduced two-dimensional model. Hence, we expect the present results to retain the essential defect physics that arises when embedding long and parallel cylindrical fibres in a nematic matrix.

2 Microstructural model for carbonaceous mesophases

The microstructual modelling of NLCs requires spatio-temporal specification of the orientation and degree of molecular order and their time evolution when driven by visco-elastic processes. Here, the microstructure is defined, the elastic energies involved in molecular distortions and the evolution equations that govern the emergence of multiscale patterns and structures. The Landau-de Gennes liquid crystal model for NLCs [7, 15, 30] is considered.

2.1 Description of microstructure

The Landau-de Gennes theory of liquid crystals, [7], describes the visco-elastic behaviour of nematic liquid crystals by using the second moment of the orientations distribution function known as the tensor order parameter $\mathbf{Q}(x, t)$ and the velocity field $\mathbf{v}(x, t)$. Further details on the modelling of orientation are given by [26]. In the absence of macroscopic flow, $\mathbf{v} = 0$, the visco-elasticity of liquid crystals is described solely by $\mathbf{Q}(x, t)$. Then, spatio-temporal changes in the order parameter may occur even in the absence of flow. In this paper, problems are considered where flow does not occur, $\mathbf{v} = 0$, and so the system is governed by $\mathbf{Q}(x, t)$. Then, reorientation-induced flow is neglected. The macroscopic and molecular description of the microstructure is defined by the second-order symmetric and traceless tensor $\mathbf{Q}$, expressed as

$$\mathbf{Q} = S\left(\mathbf{nn} - \tfrac{1}{3}\boldsymbol{\delta}\right) + \tfrac{1}{3}P(\mathbf{mm} - \mathbf{ll}). \tag{2.1}$$

In addition, the symmetric traceless order parameter $\mathbf{Q}$ may be written as an expansion of its eigenvectors:

$$\mathbf{Q} = \lambda_n \mathbf{nn} + \lambda_m \mathbf{mm} + \lambda_l \mathbf{ll}, \tag{2.2}$$

$$\lambda_n + \lambda_m + \lambda_l = 0, \tag{2.3}$$

where the uniaxial director $\mathbf{n}$ corresponds to the maximum eigenvalue $\mu_n = 2/3S$, the biaxial director $\mathbf{m}$ corresponds to the second largest eigenvalue $\mu_m = -1/3(S - P)$ and the second biaxial director $\mathbf{l}\,(= \mathbf{n} \times \mathbf{m})$ corresponds to the smallest eigenvalue $\mu_l = -1/3(S+P)$. The orientation is defined completely by the director triad $(\mathbf{n}, \mathbf{m}, \mathbf{l})$. The magnitude of the scalar order parameter S is the molecular alignment along the uniaxial director $\mathbf{n}$ and is given by $S = 3/2(\mathbf{n} \cdot \mathbf{Q} \cdot \mathbf{n})$. The magnitude of the scalar order parameter P is the molecular alignment in a plane perpendicular to the direction of the uniaxial director $\mathbf{n}$ and is given by $P = 3/2(\mathbf{m} \cdot \mathbf{Q} \cdot \mathbf{m} - \mathbf{l} \cdot \mathbf{Q} \cdot \mathbf{l})$. On the principal axis, $\mathbf{Q}$ is represented as

$$\mathbf{Q} = \begin{bmatrix} -1/3(S - P) & 0 & 0 \\ 0 & -1/3(S + P) & 0 \\ 0 & 0 & 2/3S \end{bmatrix}, \tag{2.4}$$

where $S, P \geqslant 0$ for uniaxial nematic liquid crystals. From equation (2.4), we are able to describe the state of the system by considering the region that the (S, P) duplet lies in, such as biaxial $(S \neq 0, P \neq 0)$, uniaxial $(S \neq 0, P = 0)$, $(P = \pm 3S)$ [25] and isotropic $(S = 0, P = 0)$ states. The isotropic state corresponds to the zero tensor, $\mathbf{Q} = 0$. Defects

are regions where the orientation order (S, P) sharply changes. Biaxiality may also be measured by the normalised parameter β, where $\beta \in (0, 1)$ and

$$\beta^2 = 1 - \frac{6[(\mathbf{Q} \cdot \mathbf{Q}) : \mathbf{Q}]^2}{(\mathbf{Q} : \mathbf{Q})^3}, \tag{2.5}$$

ranging from fully uniaxial, $\beta^2 = 0$, to fully biaxial, $\beta^2 = 1$. The eigenvalues of $\mathbf{Q}$ capture molecular information and the eigenvectors describe orientation, and hence, the Landau-de Gennes model is a multiscale model [20] with internal and external length scales. The biaxial parameter β is an efficient index to identify singular disclinations [8]. The typical signature of the β profile across the centre of a singular disclination is a double peak whose maximum is 1 and minimum is zero (uniaxial core). The β landscape is thus a circular ridge that separates the uniaxial far-field equilibrium domain from the uniaxial state at the centre of the defect. In this paper, we use this feature of the biaxial parameter to characterise disclination lines in FNs.

2.2 Mesophase elasticity

In the Landau-de Gennes theory, the free energy density difference between nematic and isotropic states is expressed in terms of $\mathbf{Q}$ and its spatial gradients $(\nabla \mathbf{Q})$ [37]. The total elastic free energy density, f, is given by the sum of homogeneous, f_h, and gradient, f_g, contributions:

$$f = f_h + f_g. \tag{2.6}$$

The homogeneous free energy density f_h represents the free energy difference between the liquid crystal and isotropic states and may be expressed as a power series in $\mathbf{Q}$ [20]:

$$f_h = \tfrac{1}{2} a(\mathbf{Q} : \mathbf{Q}) - \tfrac{1}{3} b(\mathbf{Q} \cdot \mathbf{Q}) : \mathbf{Q} + \tfrac{1}{4} c(\mathbf{Q} : \mathbf{Q})^2, \tag{2.7}$$

$$a = a_0(T - T^*), \tag{2.8}$$

where a_0, b and c are material constants. In the isotropic state, $f_h = 0$, and in the stable liquid crystal state, $f_h \leqslant 0$. The gradient elasticity $f_g(\nabla \mathbf{Q})$ is expressed as

$$f_g = \tfrac{1}{2} l_1 (\nabla \mathbf{Q} : \nabla \mathbf{Q}) + \tfrac{1}{2} l_2 (\nabla \cdot \mathbf{Q}) \cdot (\nabla \cdot \mathbf{Q}) + \tfrac{1}{2} l_3 \mathbf{Q} : (\nabla \mathbf{Q} : \nabla \mathbf{Q}), \tag{2.9}$$

where l_1, l_2, l_3 are constant phenomenological parameters dependent on the liquid crystal. For all states, we have the condition $f_g \geqslant 0$, and in the presence of defects, we have $f_g > 0$.

The equilibrium scalar order parameter, S_{eq}, is defined by

$$S_{eq} = \frac{b}{4c} \left[1 + \sqrt{1 - \frac{(24 a_0 c(T - T^*))}{b^2}} \right], \tag{2.10}$$

where T is the temperature within the system and T^* is the liquid crystal isotropic transition temperature. The term S_{eq} is also known as the corresponding region in the system where energy is lowest, and therefore in the absence of a defect, we have $S = S_{eq}$. Figure 3 displays S_{eq} as a function of T with material parameters corresponding to 5CB [4]. The term S_{eq} monotonically decreases with respect to T prior to entering a
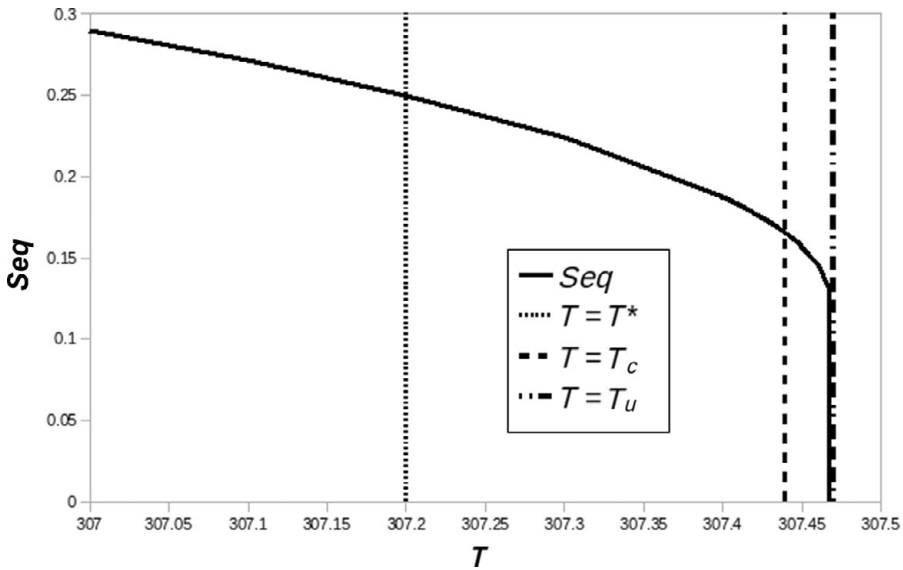
FIGURE 3. Behaviour of S_{eq} with respect to T for parameters corresponding to 5CB [4]. The vertical lines correspond to the temperatures T_c, T^* and T_u discussed in the introduction. In this paper, we study texturing in the stable phase for $T < T_c$, texturing in the metastable nematic phase for $T_c < T < T_u$ and also texturing in the unstable nematic phase for $T > T_u$.

region of T for which S_{eq} vanishes and the system lies in a stable isotropic state. This corresponds to the region of T satisfying the inequality,

$$T > T^* + \frac{b^2}{24 a_0 c},$$

corresponding to $T > 307.47$ for 5CB material parameters, indicated in Figure 3. In this temperature regime, the system is in an isotropic state as $S = 0$ throughout the domain.

This temperature regime will form an important investigation for considering fibre inclusions which impose localised ordering interactions in S.

2.3 Microstructure evolution

To describe the texture evolution, dynamical equations for the tensor order parameter must be derived. The dynamics of the system must obey the following equations:

$$\underbrace{-\gamma(\mathbf{Q}) \frac{d\mathbf{Q}}{dt}}_{\text{Viscous resistance}} = - \underbrace{\left[\frac{\delta F}{\delta Q} \right]^{[S]}}_{\text{Elastic driving force}}, \tag{2.11}$$

where the viscous resistance is due to the rotational viscosity of the mesophase and the driving force originates from a decrease in the total elastic free energy of the system where

$$F = F_h + F_g, \quad F_h = \int_V f_h \, dV \quad \text{and} \quad F_g = \int_V f_g \, dV. \tag{2.12}$$

The term γ in equation (2.11) is the rotational viscosity, $\delta F/\delta \mathbf{Q}$ is the Volterra variational derivative [10] and the superscript [s] denotes a symmetric and traceless property.

2.4 Material properties

For this investigation, the material constants corresponding to 5CB [4] are employed, namely

$$a_0 = 1.4 \times 10^5 \ (\text{J/m}^3), \quad b = 1.8 \times 10^6 \ (\text{J/m}^3) \quad \text{and} \quad c = 3.6 \times 10^6 \ (\text{J/m}^3). \quad (2.13)$$

For simplification, the rotational viscosity is kept constant such as

$$\gamma(\mathbf{Q}) = \eta = 0.084 \ \text{Pa s}.$$

An equibend–splay assumption is used resulting in l_1, $l_2 > 0$ and $l_3 = 0$, namely

$$l_1 = 3.0 \times 10^{-12} \ (\text{J/m}), \quad l_2 = 3.1 \times 10^{-12} \ (\text{J/m}) \quad \text{and} \quad l_3 = 0 \ (\text{J/m}).$$

This simplifying assumption is made on the basis of previous work; splay-bend anisotropy is a second-order effect in the present problem which does not affect the essential nature of the results [33–36].

The corresponding Frank constants, (K_{11}, K_{22}, K_{33}), representing twist and bend are given by

$$K_{11} = 6.2 \times 10^{-11} \ (\text{J/m}), \quad K_{22} = 3.9 \times 10^{-11} \ (\text{J/m}) \quad \text{and} \quad K_{33} = 6.2 \times 10^{-11} \ (\text{J/m}).$$

2.5 Geometry, auxiliary data and output vector

Results will be presented for an evolutionary texturing problem where the computational domain consists of a unit square, $(0, 1) \times (0, 1)$, with an embedded two-by-two array of circular fibres (Figure 4).

The internal boundaries are defined as the boundaries corresponding to the fibres perimeter, and the external boundaries correspond to the boundaries associated with the square. The geometric composition is such that for a square of width, W, the distance between fibre centres along a horizontal or vertical plane is equal to $(1/2W)$, and the distance between a fibre centre to its nearest external boundary is equal to $(1/4W)$. The equations are solved within the bulk of the system only (outside the internal domain of the fibres). In our case, the ratio of domain width, W, to fibre radius, R, is given by $(W/R) = 20$.

In every computation, the application of initial conditions and internal boundary conditions is constant, namely

Initial conditions

$\mathbf{Q} = 0$ throughout the domain (isotropic).
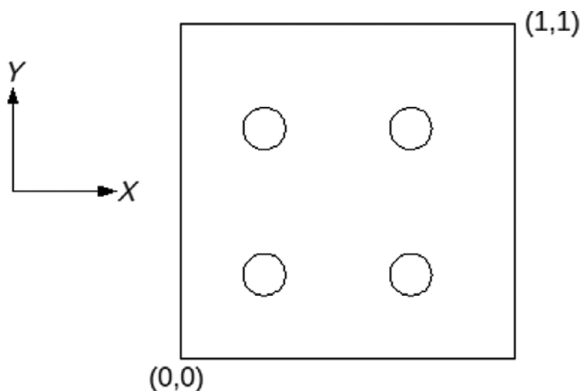
Internal boundary conditions

FIGURE 4. Schematic of the computational domain consisting of a square lattice of four fibres embedded within a unit square, $(0, 1) \times (0, 1)$. Internal boundaries are defined as the boundaries corresponding to the fibre perimeters, and external boundaries correspond to the boundaries associated with the square. The domain is such that for a square of width W, the distance between fibre centres along a horizontal or vertical plane and from fibre centre to its nearest external boundary is equal to $(1/2W)$ and $(1/4W)$, respectively. In this problem, the ratio of width, W, to fibre radius, R, is given by $(W/R) = 20$.

Dirichlet conditions in $\mathbf{Q}$, namely

$$q_{ij} = S_{eq}(\mathbf{N}_i \mathbf{N}_j - 1/3\boldsymbol{\delta}), \tag{2.14}$$

where $\mathbf{N} = (\mathbf{N}_i, \mathbf{N}_j)$ is a unit vector normal to the boundary surface. Note from equation (2.10) that this is a temperature-dependent expression. In this case, an initially isotropic system is influenced by a localised order interaction with a long range effect causing an evolutionary texturing process. With this constant methodology, the evolution of the texturing process is considered by quenching the isotropic state to the nematic state at different T. The governing equations (2.11) and (2.12) are a set of five non-linear PDE's, and the solution vector is $Q(x, t)$. The equations are solved in dimensionless form. Time and space are scaled as follows:

$$a^* = a_0 \overline{T}, \quad b^* = \frac{b_o}{a_0 T^*}, \quad c^* = \frac{c_0}{a_0 T^*},$$

$$l_1^* = \frac{l_1}{l^2 a_0 T^{*2}}, \quad l_2^* = \frac{l_2}{l^2 a_0 T^{*2}}, \quad \overline{T} = \frac{T - T^*}{T^*}, \quad t^* = \frac{\mu}{a_0 T^*}, \tag{2.15}$$

where l is the simulation-specific imposed length scale and the asterisk represents non-dimensionality. For convenience, this notation is dropped.

Since the model is made dimensionless, it is instructive to translate the spatial dimensionless scales into real scales. The temperature-dependent correlation length of a defect core, $\epsilon(T)$, is given as

$$\epsilon(T) = \sqrt{\frac{l_1}{a}}. \tag{2.16}$$

For 5CB at $T = 307.3$ K, the scale of a defect core radius is $\epsilon \approx 1.46 \times 10^{-8}$ m. Using representative results at this temperature, we find that the box size, the fibre radius, R, and the centre-to-centre fibre distance are $\approx (34.24\epsilon, 1.71\epsilon, 17.12\epsilon)$, respectively.

Finite element software (COMSOL Multiphysics) [5] is employed for all computations where a static mesh is used for each simulation. Convergence, mesh independence and accuracy were implemented using standard numerical procedures.

In practice, it is feasible to place fibres in a regular array experimentally as discussed by Gupta, Hwang and Rey [17].

2.6 External boundary conditions and fibre arrangement

A large theme of this paper is to present results for the cases of two different types of conditions imposed on the external boundaries which create two clearly distinct physical problems. In the first case, we apply periodic conditions in some terms, namely

$$\mathbf{Q} \text{ and } \mathrm{grad}(\mathbf{Q}) = \left(\frac{\partial \mathbf{Q}}{\partial x}, \frac{\partial \mathbf{Q}}{\partial y} \right). \tag{2.17}$$

Periodicity of the terms in equation (2.17) creates the effect that the computational domain is replicated over an infinite displacement in the horizontal and vertical planes dually. Then, the situation of an infinite lattice is solved.

In the second case, Dirichlet conditions are placed on the external boundaries, namely

$$q_{ij} = S_{eq}(\mu_i \mu_j - 1/3\delta) \quad \text{where} \quad \mu = (0, 1). \tag{2.18}$$

Equation (2.18) imposes a far-field effect where the texturing process is bounded with the imposition of a vertical director.

Hence, one key goal of this paper is to establish the fundamental differences when applying these two different conditions on the external boundaries, equations (2.17) and (2.18), which generate these two distinct physical situations.

2.7 Determination of temperature gap to observe higher-order unsplit defects

In this paper, the defect splitting mode is observed as a function of temperature and given fibre radius size for an ensemble of fibres with quadrilateral symmetry. The previous work of Gupta and Rey [37] has predicted the phase transition line between defect split and non-split with respect to temperature and fibre radius, as described by equation (1.2). The transition criterion is geometry dependent at lower fibre sizes and temperature dependent at greater fibre sizes. This predicted behaviour may be extended to a fibre ensemble with quadrilateral symmetry by using a three parameter power law model as

$$T_u - T_s = \frac{a}{(R/\epsilon - b)^n}, \tag{2.19}$$

where T_s represents the greatest temperature for which defect splitting occurs, a, b and n are parameters representing the curves vertical and horizontal displacement and concavity, respectively. The left-hand term of equation (2.19) represents the temperature gap between

T_u and T_s. This has the limits

$$\lim_{R/\epsilon \to b} (T_u - T_s) = \infty \quad \text{and} \quad \lim_{R/\epsilon \to \infty} (T_u - T_s) = 0.$$

2.7.1 Analysis of touching fibres

For a quadrangular arrangement of touching fibres of radius R, the radius of the inner gap is equal to $R_h = 0.414R$. Then, the maximum temperature gap observed for this fibre ensemble is given by

$$\max\{T_u - T_s\} = \frac{a}{(0.414R/\epsilon - b)^n}.$$

Assuming that $1K$ is the limit beyond which fluctuations are not important, i.e. $\max\{T_u - T_s\} = 1$, the maximum fibres size that may be used for touching fibres is

$$R_{max} = 2.41\epsilon((a)^{1/n} + b).$$

2.7.2 Analysis of non-touching fibres

Here, we consider a square fibre arrangement with constant lattice L and with fibres of radius R. In this case, we find that the radius R_h of the enclosed lattice is given by

$$R_h = \frac{\sqrt{2}L}{2} - R.$$

Replacing this expression into the power law model given in equation (2.19) provides

$$T_u - T_s = \frac{a}{((\sqrt{2}L/2 - R)/\epsilon - b)^n)} = \frac{a\epsilon^n}{((\sqrt{2}L/2 - R) - \epsilon b)^n}.$$

The value of the fibre radius that will give a transition at a given T_s for a lattice constant L is

$$R = \frac{\sqrt{2}L}{2} - \epsilon \left(\left(\frac{a}{T_u - T_s} \right)^{1/n} + b \right).$$

Then, we have the following rules:

(1) For a given L, the larger $(T_u - T_s)$ is required, the larger value of R is required.

(2) For a given R, the larger $(T_u - T_s)$ is required, the smaller L is required.

(3) For a fixed $(T_u - T_s)$, the greater L, the greater R is required to split the defect.

Then, in summary, to maximise the temperature gap at which we have a defect splitting event, we have

$$\max\{T_u - T_s\} = \frac{a\epsilon^n}{\min\{((\sqrt{2}L/2 - R) - \epsilon b)^n\}}.$$

In order to minimise the denominator, we require

$$\frac{\sqrt{2}L}{2} - R \approx \epsilon b = \text{constant} \approx 100 \text{ nm}.$$

Then if we choose

$$R \approx \frac{\sqrt{2}L}{2} - 100 \text{ nm},$$

we will obtain a large temperature gap. In this paper, we use $L/H = 0.5$ and $R/H = 0.05$ where H is the box size. Under these conditions, $(T_u - T_s)$ is then small, but the results derived in this section show how to modify the geometry (L, R) to increase $(T_u - T_s)$. An example of this technique is provided in Figure 13.

If we consider the term

$$N = \frac{\sqrt{2}}{2} \frac{L}{\epsilon} - \frac{R}{\epsilon} = b,$$

then for $N \to 10$ from above, large temperature gaps may be obtained. From simulations given in Figure 6(c), $R/\epsilon \approx 3$, $L/\epsilon \approx 30$ and so $N \approx 20$. Then, these simulations will generate small temperature gaps.

3 Results and discussions

Sections 3.1 and 3.2 discuss results with the applied periodic and Dirichlet conditions imposed on the external boundaries respectively and for temperatures corresponding to stable nematic phases. Section 3.3 discusses an alternative methodology where the fibre surfaces impose a localised ordering effect in S and nucleate defect structures in a regime of temperature for which the system would normally lie within an isotropic state and $S_{eq} = 0$. As mentioned above, we use β to visualise topological defects with a grey scale defined by black ($\beta = 0$) and white ($\beta = 1$) such that a disclination under circular confinement appears as a white ring. To include the full fibre arrangement, the ensuing visual (not computational) resolution will give a white dot instead of a ring. Furthermore, owing to the complex fibre embedding, the classical ring-like domain may be distorted to other shapes.

3.1 Periodic conditions

On the basis of previous work [14, 17] for an infinite periodic square fibre lattice, we expect an infinite array of disclinations whose charge per lattice is $+4$. In addition, we also expect a centreline $+1$ disclination to exist only close to the NI transition but split at lower T.

Figure 5(a) displays the biaxial parameter β grey-scale visualisation obtained at steady state for $T = 307.37$. At the centre region, we find an asteroid (star-shaped) disclination encircled by a ring along the perimeter reflecting the boundary condition periodicity. At this T, the structure's topology remains constant, and this is the lowest critical temperature which does not result in a defect splitting at the centre. Figure 5(b) displays the corresponding director field.

This is in contrast to the situation for $T = 307.36$. Figure 6 displays the β profile at different stages of the computation, (a),(b) and (c), at $t = 6 \times 10^3, 1.2 \times 10^5, 5 \times 10^5$, respectively. Here, the biaxial asteroid and the biaxial ring are formed at the initial time steps, but at this lower T, a topological change occurs in β and the centre region asteroid splits into two $+1/2$ defects that move towards the fibre boundaries; the peripheral ring
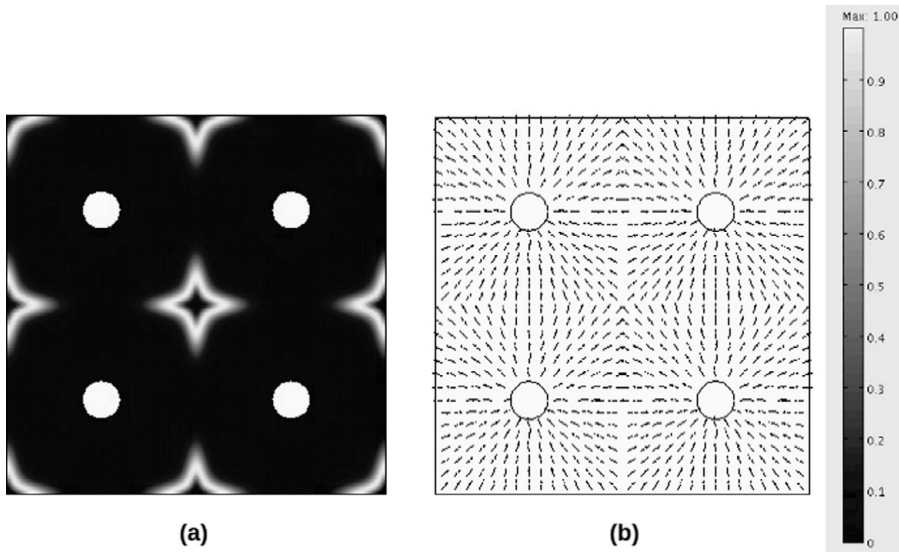
FIGURE 5. The biaxial parameter, β, obtained with applied periodic external boundary conditions as a steady state solution for $T = 307.37$, $t = 10^6$, is presented in (a). The asteroid-star-shaped disclination obtained in the centre remains fixed for this temperature. The corresponding director field is presented in (b).
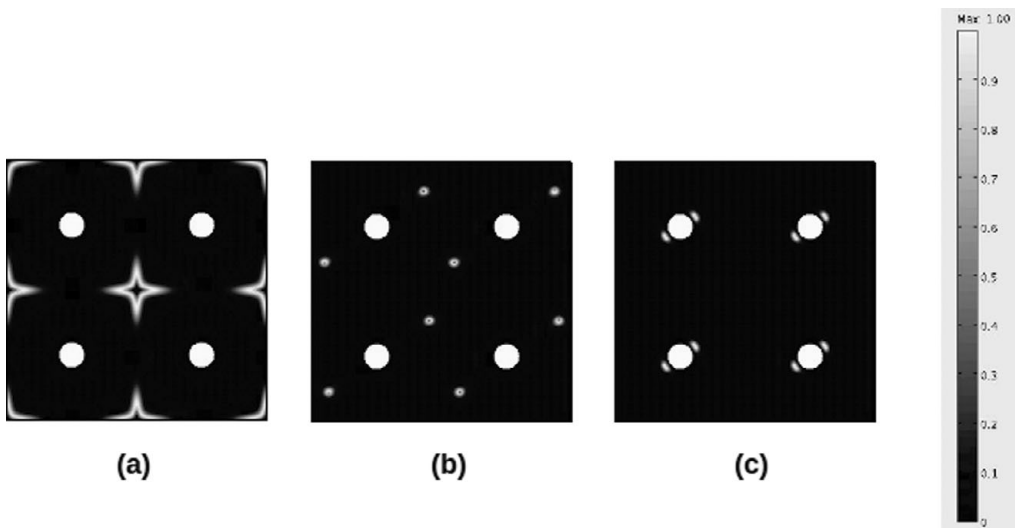

FIGURE 6. The biaxiality parameter β obtained with periodic external boundary conditions, $T = 307.36$, at different time steps, (a), (b) and (c), corresponding to $t = (6 \times 10^3, 1.2 \times 10^5, 5 \times 10^5)$ respectively. The biaxial asteroid forms at low t prior to splitting into two $+1/2$ defects propagating towards the fibre boundaries.
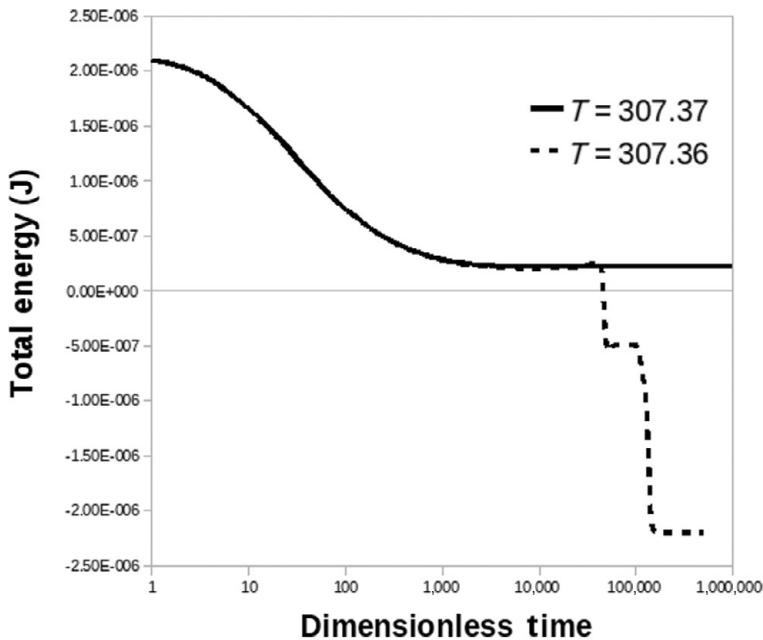
FIGURE 7. Evolution of total energy, equation (2.12), for $T = 307.37$ and $T = 307.36$, periodic external boundary conditions. These temperatures represent the critical transition point for which the asteroid-shaped region of biaxiality splits into two defects.

breaks and forms six $+1/2$ defects. The net topological charge inside the computational box is $(8 \times (+1/2) = +4)$. Hence, the system possesses a clear topological transition in structure when below the critical temperature (Figure 5) by a numerical factor $(= 10^{-5})$.

For all T below this critical transition temperature, the same observed topological change and the final steady state solution are observed with the regime changes occurring at smaller time steps for decreasing T.

The regime change (Figures 5–6c) is characterised by the evolution of the total energy shown in Figure 7 for $T = 307.36$ and $T = 307.37$, corresponding to the two cases. The figure shows that the total free energy follows an initial monotonic decay that reaches a plateau. The lower T regime displays two sharp drops separated by an intermediate plateau.

At a dimensionless time $t = 44719$, the first plateau is reached, and there is a split in which the energy of the lower temperature texture decreases but the higher temperature texture remains invariant. The split in energy between the high and low T regimes is due to the breakage of the centre asteroid and the peripheral filament into four disclinations. Once the high T texture with eight disclinations reaches the second plateau, disclination/disclination and disclination/fibre repulsion and attraction forces further coarsen the texture such that each fibre is surrounded by two $+1/2$ disclinations (see Figure 6c).

Figure 8 shows the total free energy temporal evolution for $T = 307.3$ (low T regime) and the corresponding grey-scale visualisation of the uniaxial scalar order parameter S, where black denotes $S = 0$ and white denotes $S = S_{eq}$. The figure clearly captures how
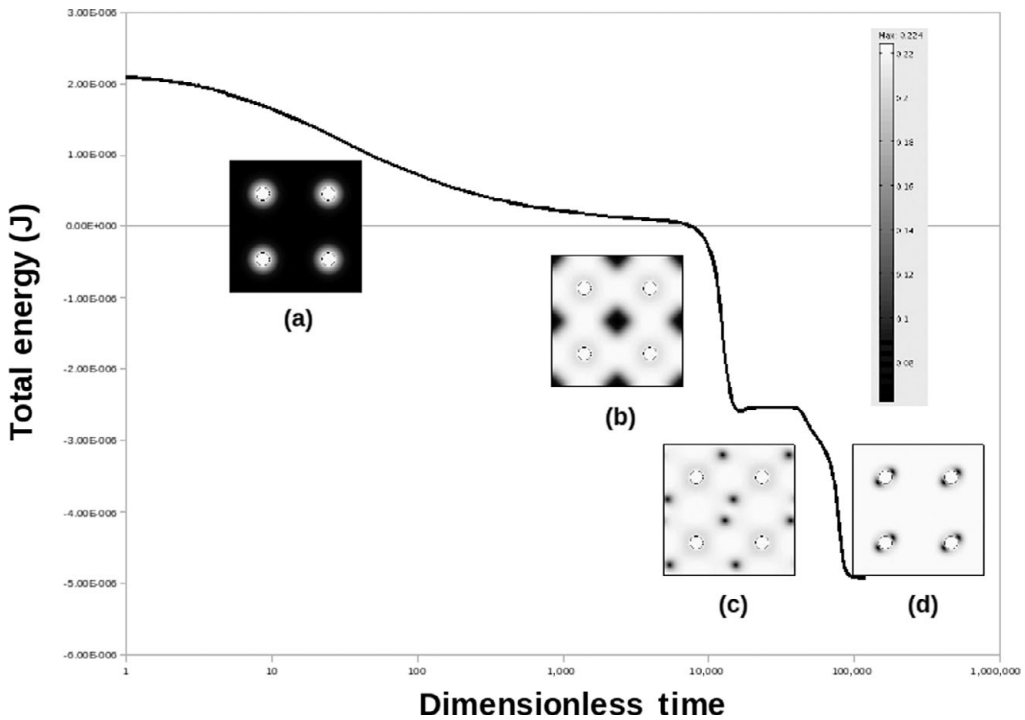
FIGURE 8. Evolution of total energy and time for $T = 307.3$, periodic external boundary conditions and corresponding grey-scale visualisations of S. The profiles of S corresponding to (a),(b),(c) and (d) indicate clear transformations within the system such as isotropic $\rightarrow$ asteroid and peripheral filament defects $\rightarrow$ nucleation of $8 \times (+1/2)$ defects $\rightarrow$ defect relocation $\rightarrow$ quadruple single fibre + two defect at steady state.

the matrix undergoes the following textural transformation: isotropic $\rightarrow$ asteroid and peripheral filament defects $\rightarrow$ nucleation of $8 \times (+1/2)$ defects $\rightarrow$ defect relocation $\rightarrow$ quadruple single fibre + two defect at steady state.

3.2 Dirichlet conditions

Results are considered where the boundary conditions assigned on the external boundaries are of Dirichlet type (equation (2.18)). Similar to section 3.1, the regime of T is considered such that S_{eq} is positive. Figure 9 displays the steady state solutions for β for the data sets $T = (307.46, 307.45, 307.44, 307.43)$, corresponding to the critical regime prior to defect break-up at $T = 307.42$ (Figure 11). The lower symmetry of the textures of four fibres embedded in an aligned nematic matrix when compared with an infinite fibre lattice is evident when comparing Figures 5 and 9. The asteroid defect in the periodic case now becomes an asteroid attached vertically to two Y-shaped domains; similarly, the peripheral defect ring (see Figure 5) becomes a heterogeneous, segmented series of domains. In terms of rotational symmetries, the periodic fibre lattice case has a $\pi/2$ identity, but the Dirichlet has a π identity. This is due to the vertically aligned orientation at the boundary of the latter.
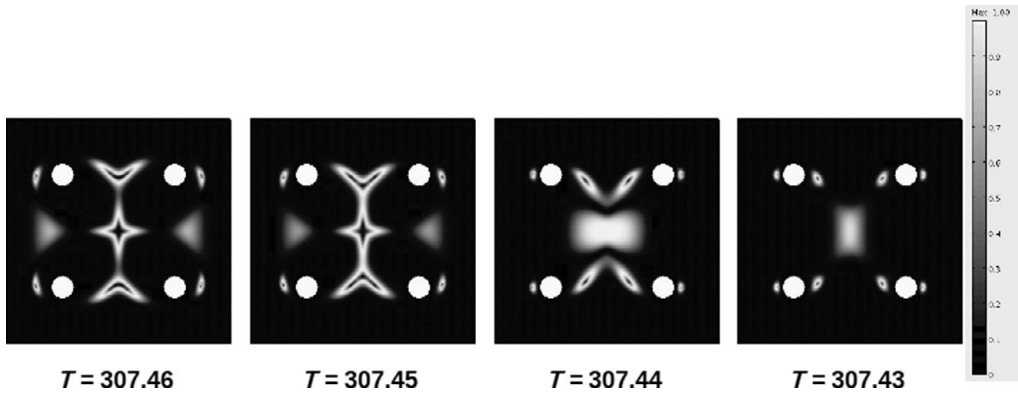
FIGURE 9. Profiles of β for $T = (307.46, 307.45, 307.44, 307.43)$ at $t = 10^6$ and Dirichlet external boundary conditions. This temperature range corresponds to the critical regime prior to defect break-up corresponding to $T = 307.42$. There is lower symmetry associated with four fibres embedded in an aligned nematic matrix compared with the case of an infinite lattice (Figure 5).

In contrast to the case of periodic boundary conditions, the break-up regime occurs at higher T and is continuous when the β profile changes topology prior to break-up. Figure 10 shows the β profiles for $Y = 0.5$ across the centre section of the computational domain corresponding to Figure 9. At high T ($T = 307.46$), the β profile has the usual double peak associated with a disclination. As T increases, the two peaks merge into a large peak ($T = 307.44$), and a further decrease in T leads to a narrow biaxial single peak at $T = 307.43$. It is emphasised that the textures shown in Figure 9 are at steady state and the continuous nature of the texture transformation refers to the temperature change. This temperature corresponds to the pre-transitional defect splitting temperature that occurs at $T = 307.42$ K, and at this temperature, the texture is composed of four outer $+1/2$ disclinations and inner regions with a large biaxial rectangular domain linked to four small biaxial ellipses.

Figure 10 shows that at $T = 307.46$, β replicates the classic profile of a defect structure, where $\beta = 0$ in the defect centre and rises to two peaks of $\beta = 1$. Decreasing the temperature generates a transformation from a double peak to a single peak in β.

Figure 11 displays the texture formation for $T = 307.42$. The defect structure enters a topological transition and splits as in Figure 11(a), $t = 3.65 \times 10^4$, and defects propagate towards the fibre boundaries as in Figure 11(b), $t = 1.2 \times 10^5$. This is an identical result to the situation of periodic boundary conditions (Figure 6). Then, it is apparent that the final steady state solution at lower T is independent from the applied external boundary conditions. The structure formation is sensitive to the nature of boundary conditions for high T only prior to defect break-up. The structure in both cases will undergo a transition from a collective mode (defects are shared by the four fibres) to a single-fibre mode (each fibre is surrounded by two defects), which must be insensitive to matrix and boundary conditions.

Comparing Figures 8(d) and 11(b), it is clear that the external boundary conditions solely influence the collective modes that arise at higher temperatures. In characterising the system and the accuracy of the model, the distribution of gradient energy, F_g, may
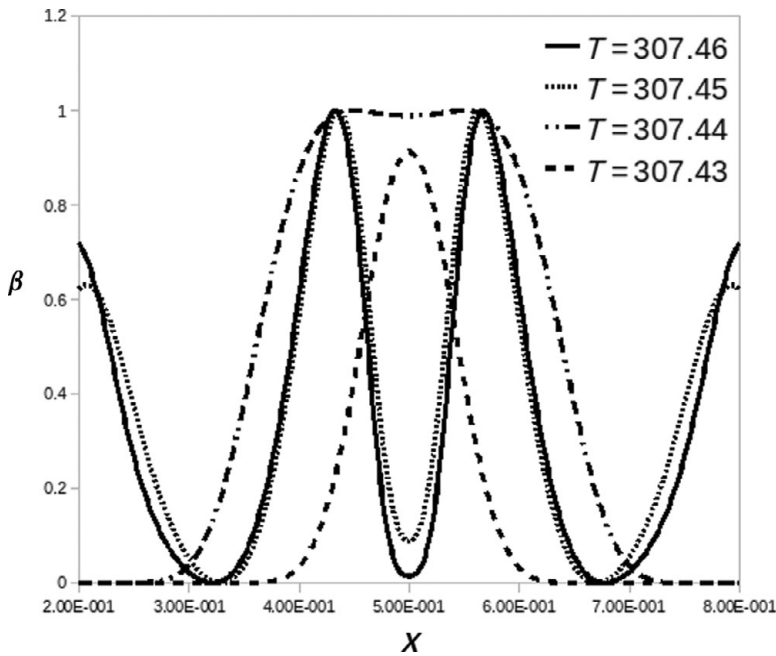
FIGURE 10. Cross-section profiles of β ($X \in (0.2, 0.8)$, $Y = 0.5$) for $T = (307.46, 307.45, 307.44, 307.43)$, $t = 10^6$ and Dirichlet external boundary conditions. The profile undergoes rapid changes with respect to T such as forming the usual double peak associated with a disclination for $T = 307.46$, merging into a large peak, $T = 307.44$, and forming a narrow biaxial peak, $T = 307.43$.
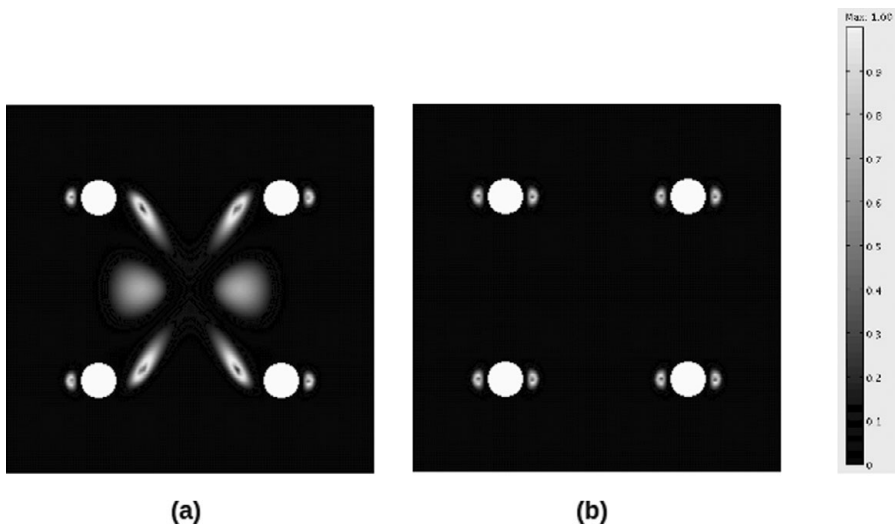

FIGURE 11. Profile of β for $T = 307.42$ where (a) and (b) correspond to $t = (3.65 \times 10^4, 1.2 \times 10^5)$, respectively and Dirichlet external boundary conditions. There is a clear topological transition at this temperature where the asteroid region splits and defects propagate towards the fibre boundaries. This is in agreement with the situation in Figure 6.
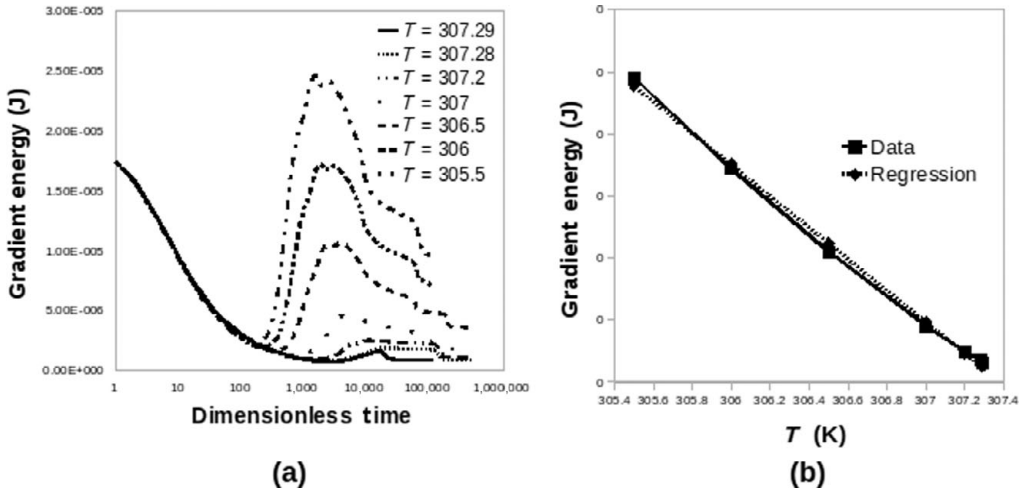
FIGURE 12. Profiles of F_g as a function of t for varying T and applied Dirichlet external boundary conditions are presented in (a). A linear regression for (T, F_g) is presented in (b).

be considered and also the change in F_g required for structure break-up for varying T. From theory, the relationship between the Landau-de Gennes and Frank constants are given by [29]:

$$l_1 = \frac{k_{22}}{2S_{eq}^2}, \quad l_2 = \frac{k_{11} - k_{22}}{S_{eq}^2},$$

and from

$$S_{eq}^2 \propto \frac{1}{T},$$

there is the established theoretical prediction that at higher T, less energy is required to break up the elasticity of the structure and the magnitude of energy required $\propto(1/T)$.

This result is established within the simulations (Figure 12), which displays the magnitude of F_g released on defect break-up, decreasing with T (Figure 12(a)) and a plot of the total gradient energy as a function of T for (T, F_g) (Figure 12(b)).

Over this small range of temperature, the plot is linear but may generate a curved profile over greater ranges of temperature.

Figure 13 displays the biaxial structure obtained for $T = 307$ within this different arrangement of smaller fibres that are situated in nearer proximity such that $L/H = 0.1$ and $R/H = 0.03$. It is evident that this new arrangement is able to maintain biaxial structures at lower temperatures, then increasing $(T_u - T_s)$. This result provides an example of the theory discussed in section 2.7.

3.3 Surface-induced ordering effects

For temperatures in which the nematic phase is unstable ($T > T_u = 307.47$), no bulk ordering is expected. Nevertheless, surface-induced ordering may arise from strong interactions between the fibre and the mesophase [23, 31], a case known as surface-induced ordering. This section seeks to demonstrate that surface-induced ordering in FN may also create
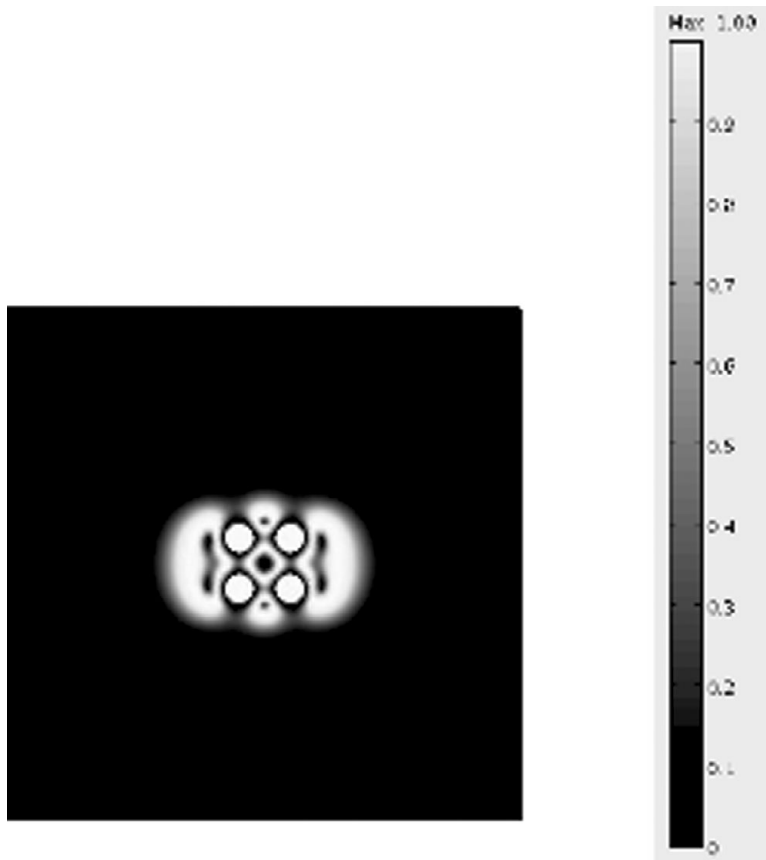
FIGURE 13. Profile of β for $T = 307$ and $t = 10^6$. Here the splitting temperature has been clearly lowered because of the effect of reducing the fibre distance and radius. In this case, $L/H = 0.1$ and $R/H = 0.03$.

texturing in the bulk through the gradient elasticity that propagates order and orientation from the internal surfaces. Since the propagated orientation carries the fibre curvature information, we expect that defect-like structures will nucleate through the frustration effect. To capture surface-induced ordering, we use the following Dirichlet condition on the internal surfaces:

$$q_{ij} = \alpha(\mathbf{N}_i\mathbf{N}_j - 1/3\boldsymbol{\delta}), \qquad (3.1)$$

where α is a constant arising from the surface-induced ordering. Equation (3.1) is identical to equation (2.14) with the exception of the S_{eq} term being replaced by α. This modification removes dependence of T, and when in the regime of T for which the system lies in a naturally isotropic state, a localised ordering interaction may be nucleated by applying equation (3.1) as the internal Dirichlet conditions and considering $\alpha \gg 0$.

It is clearly noted that this methodology is physically different from that discussed in sections 3.1 and 3.2 where the fibres nucleated defects through a distortion in the director field and not the ordering parameter. Results will be considered in the regime of T for which $(\mathbf{Q} = 0, S = 0)$ is the natural state. Results will be considered with the application of
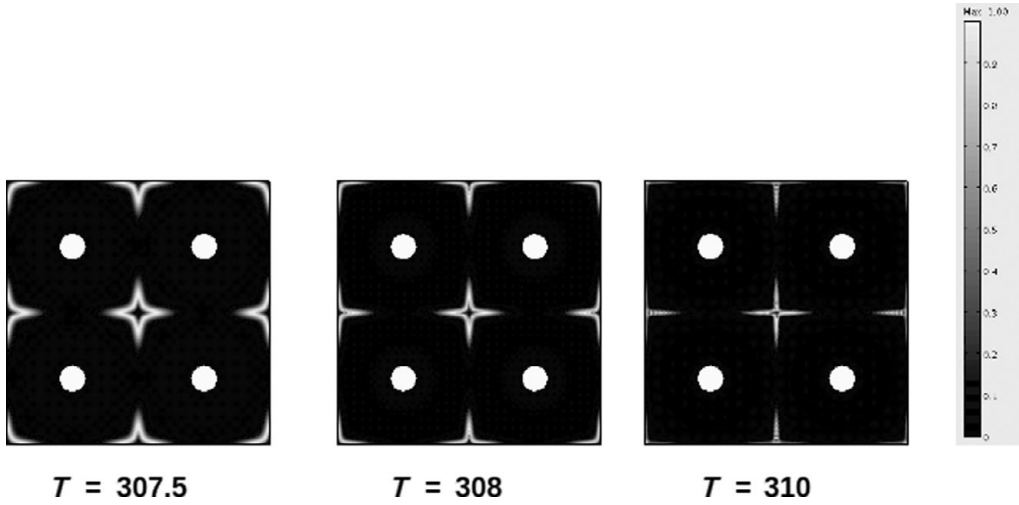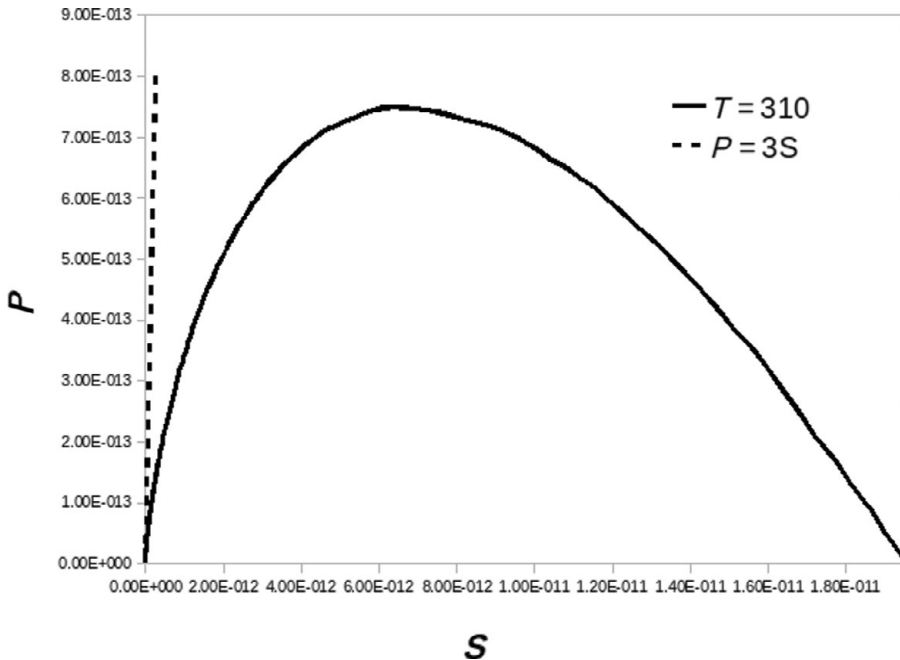
FIGURE 15. Cross-section (S, P) profile $(X \in (0.5, 1),\ Y = 0.5)$, periodic external boundary conditions, $T = 310$, $S_{eq} = 0$ and $t = 10^6$. The profiles intersect with the lines $(S = 0)$ and $(P = 3S)$. The latter case corresponds to the core of the defect in the centre.

periodic boundary conditions imposed on the external boundaries as defined in equation (2.17).

Figure 14 displays the profiles of β obtained at steady state for $T = (307.5, 308, 310)$. In each case, $\alpha = S_{eq}|_{T=T^*} \approx 0.19$. The star-shaped region of biaxiality is obtained in all cases similar to the profiles obtained in Figure 5. Then, there is the clear result that the concept of imposed localised ordering takes effect within systems which will naturally lie in an isotropic state.

There is an apparent reduction in the biaxiality region with increasing T as the star-shaped cluster is forming higher gradients, indicating that the gradient energy is becoming less costly.

Surface-induced ordering creates a boundary layer around each fibre, but the value of S in the bulk shows localised heterogeneities as shown in Figure 14. To characterise the order in this defect mesh, we can use the trajectory in the $S - P$ plane. As is known [9], defects cores lie on the $(P = 3S)$ uniaxial line on which $\beta = 0$.

Figure 15 shows the trajectory on the $S - P$ phase plane and the $(P = 3S)$ uniaxial line, showing that at the centre of the computational domain ($x = 0.5, y = 0.5$), the nematic order is uniaxial as in normal disclinations (although not shown, the actual values of S and P are small but not zero). In partial summary, surface-induced ordering in a periodic FN results in a defect mesh structure that does not penetrate the fibres.

The mesh thins out with increasing temperature, and the order at the mesh nodes obeys the uniaxial defect rule $P = 3S$ found in the nematic temperature range.

4 Conclusions

In this paper, a two-dimensional simulation on the Landau-de Gennes equations has been employed to characterise the influence of temperature on defect structures arising in fibre-filled nematics. The theme of this research may be regarded broadly as being divided into two physically different investigations due to the regime of temperature. In the first case, the temperature is low enough for non-zero ordering parameters to exist, $S_{eq} > 0$, and in the second case, a natural isotropic state would occur, $S_{eq} = 0$.

Firstly, the investigations at lower temperatures are considered, $S_{eq} > 0$. In this regime, the problem is investigated for two physically different types of boundary conditions imposed on the external boundaries of the computational domain. In one case, periodic boundary conditions are imposed, creating a repeating fibre lattice. In the second case, Dirichlet conditions are imposed, representing a far-field aligned director orientation effect. The same methodology is applied in each case with the same temperature-dependent expression applied as Dirichlet conditions in $\mathbf{Q}$ on the internal boundaries. For a given T, the texture formation is evolved from the same initial conditions ($\mathbf{Q} = 0, S = 0$).

The evolution of texture formation is considered through a temperature sweep.

Figure 16 displays a schematic illustrating the steady state solutions observed for β with varying T and the two external boundary conditions. In both cases, there is a clear transition change in the defect structures with respect to temperature with an initial cluster of biaxiality forming as steady state solutions at higher temperatures, (b) and (e). There is an evident transition regime in temperature for which this region of biaxiality will break into defects of lower strength that move towards the fibre boundaries, (a) and (c). The
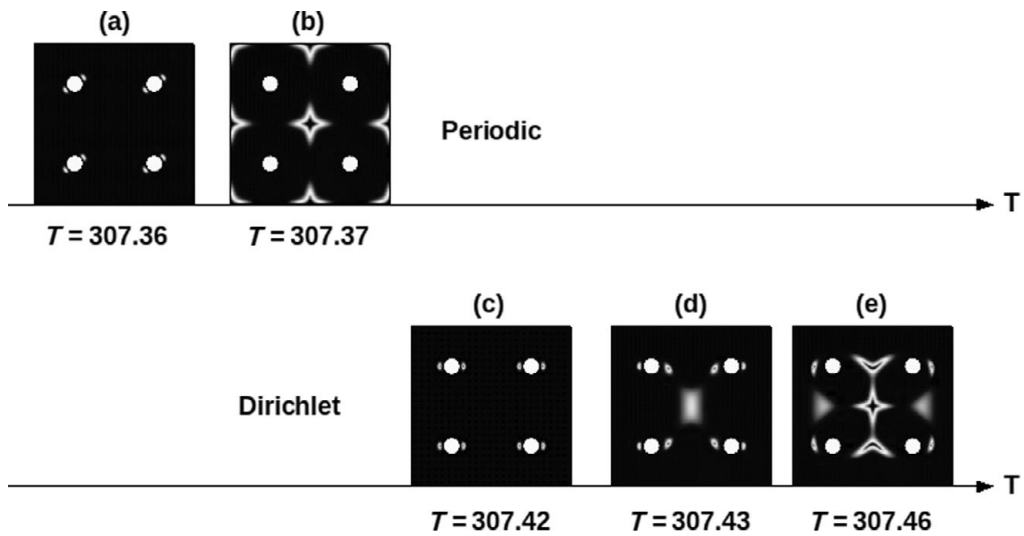
FIGURE 16. Schematic of β structures at steady state solutions ($t = 10^6$) with respect to T for applied periodic and Dirichlet external boundary conditions, $S_{eq} > 0$ in each case. There is a clear transition in the defect structures in both cases with clusters of biaxiality forming at higher T. There is a transition regime where the biaxiality cluster splits into defects of lower strength that move towards the fibre boundaries. At lower T, there is exact agreement between the two boundary condition types.

nature of external boundary conditions clearly contributes a significant difference to the behaviour of defect structure with respect to T. The transition temperature for defect break-up varies considerably between the periodic and Dirichlet cases. In the former, the defect structure exhibits an abrupt transition from a steady state region of biaxiality to the defect splitting stage due to a numerical difference in temperature ($= 10^{-5}$). In the latter case, the transition is continuous where the steady state biaxiality region displays the classic β structure at higher temperatures, continuously changing topology, (d), prior to entering the regime of defect break-up. The primary rotational symmetry angle between the two cases, (b) and (e), varies from ($\pi/2$) to π respectively.

At the lower values of T, there is exact agreement between the two boundary conditions, (a) and (c). In this regime, there is a transition from a collective mode to a single-defect mode which is insensitive to the matrix and external boundary conditions. In this regime, each fibre is surrounded by two defects, different from the situation of collective mode associated with higher temperatures. In summary, the influence of external boundary conditions on the steady state solution has affect at the higher temperature ranges solely, prior to the nucleation of defect break-up and single-fibre mode defects.

This investigation has been complimented by considering the surface-induced ordering at temperature regimes for which the system would normally remain isotropic. Dirichlet conditions have been imposed on the internal boundaries such that ($\mathbf{Q} \neq 0$), and this has generated a clear boundary layer within the ordering parameter across the domain. Thin defect lattice structures have been nucleated within these systems that would normally remain isotropic, which indicates the propagation of localised ordering on fibre surfaces

through the bulk of the domain. The observed defect is a mesh-like localised structure whose nodes obey the classical $P = 3S$ uniaxial rule that prevails at lower temperatures.

Acknowledgement

References

[1] ARAKI, T., TOJO, K., FURUKAWA, A. & ONUKI, A. (2009) Defect structures in nematic liquid crystals around charged particles. *Eur. Phys. J.* **30**, 55–64.

[2] BRANDAC, Z., SVETEC, M., KRALIJ, S. & ZUMER, S. (2006) Anhilation of nematic point defects: Pre-collision and post-collision evolution. *Eur. Phys. J.* **20**, 71–79.

[3] CHANDRASEKHAR, S. (1986) The structures and energetics of defects in liquid crystals. *Adv. Phys.* **35**, 507–596.

[4] COLES, J. H. (1978) Laser and electric field induced birefringence studies on cyanobphenyl homologs. *Mol. Cryst. Liq. Cryst.* **49**, 67–74.

[5] COMSOL. (1998) Multiphysics, modelling and simulation [online]. URL: http://www.comsol.com.

[6] DE ANDRADE LIMA, L. R. P., GRECOV, D. & REY, D. A. (2006) Multiscale theory and simulation for fiber precursors based on carbonaceous mesophases. *Plast., Rubbers Compos.* **35**, 276–286.

[7] DE GENNES, P. G. & PROST, J. (1993) *The Physics of Liquid Crystals*, Clarendon, Oxford.

[8] DE LUCA, G. & REY, D. A. (2007) Point and ring defects under capillary confinement. *J. Chem. Phys.* **127**(104902), 1–11.

[9] DE LUCA, G. & REY, D. A. (2007) Ring-like cores of cylindrically confined nematic point defects. *J. Chem. Phys.* **126**(094907), 1–11.

[10] FRIEDEL, J. (1967) *Dislocations*. Pergamon, Oxford.

[11] FUKUDA, J. & YOKOYAMA, H. (2001) Direct configuration and dynamics of a nematic liquid crystal around a two dimensional spherical particle: Numerical analysis using adaptive grids. *Eur. Phys. J.* **4**, 389–396.

[12] GRECOV, D. & REY, D. A. (2006) Texture control strategies for flow-aligning liquid crystal polymers. *J. Non-Newton. Fluid Mech.* **139**, 197–208.

[13] GUPTA, G. & REY, D. A. (2005) Texture modeling in carbon–carbon composites based on mesophase precursor matrices. *Carbon* **43**, 1400–1406.

[14] GUPTA, G. & REY, D. A. (2005) Texture rules for filled nematics. *Phys. Rev. Lett.* **95**(127802), 1–4.

[15] HESS, S. & SONNET, A. (1995) Alignment tensors versus director: Description of defects in nematic liquid crystals. *Phys. Rev.* **52**, 718–722.

[16] HOGAN, J. S. & MOTTRAM, J. N. (1997) Disclination core structure and induced phase change in nematic liquid crystals. *Phil. Trans. Soc.* **355**, 2045–2064.

[17] HWANG, K. D., GUPTA, G. & REY, D. A. (2005) Optical and structural modeling of disclination lattices in carbonaceous mesophases. *J. Chem. Phys.* **122**(034902), 1–11.

[18] KIM, W. M., BOAMFA, I. M. & RASING, H. T. (2003) Observation of surface and bulk phase transitions in nematic liquid crystals. *Nature* **421**, 149–152.

[19] KLEMAN, M. (1982) *Points, Lines and Walls: In Liquid Crystals, Magnetic Systems and Various Ordered Media*, John Wiley and Sons, New York.

[20] KLEMAN, M. & LAVRENTOVICHM, D. O. (2009) *Soft Matter Physics: An Introduction*, Springer Wien, New York.

[21] MOTTRAM, J. N. & SLUCKIN, J. T. (2000) Defect-induced melting in nematic liquid crystals. *Liq. Cryst.* **10**, 1301–1304.

[22] NEYTS, K., BAETS, R. & DESMET, H. (2005) Modeling nematic liquid crystals in the neighborhood of edges. *J. Appl. Phys.* **98**(123517), 1–6.

[23] NOBLE-LUGINBUHL, A. R., BLANCHARD, R. M. & NUZZO, R. G. (2000) Surface effects on the dynamics of liquid crystalline thin films in nanoscale cavities. *J. Am. Chem. Soc.* **122**, 3917–3926.

[24] OSWALD, P. & PIERANSKI, P. (2005) *Nematic and Cholesteric Liquid Crystals: Concepts and Physical Properties Illustrated by Experiments,* Taylor and Francis, New York.

[25] REY, D. A. (1995) Bifurcational analysis of the isotropic-nematic phase transition of rigid rod polymers subjected to biaxial stretching flow. *Macromol. Theory Simul.* **4**, 857–872.

[26] REY, D. A. (1995) Macroscopic theory of orientation transitions in the extension flow of side-chain nematic polymers. *Rheol. Acta* **34**, 119–131.

[27] REY, D. A. (2007) Capillary models for liquid crystal fibers, membranes, films and drops. *Soft Matter* **3**, 1349–1368.

[28] REY, D. A. & YAN, J. (2003) Modelling elastic and viscous effects on the texture of ribbon shaped carbon fibers. *Carbon* **41**, 105–121.

[29] SCHIELE, K. & TRIMPER, S. (1983) On the elastic constants of a nematic liquid crystal. *Phys. Stat. Sol. (b)* **118**, 267–274.

[30] SCHOPOL, N. & SLUCKIN, J. T. (2007) Landau-de Gennes theory of isotropic–nematic–smectic liquid crystal transitions. *Phys. Rev. Lett.* **75**(051707), 1–11.

[31] SOKOLOVSKA, G. T., SOKOLOVSKII, O. R. & PATEY, N. G. (2004) Surface induced ordering of nematics in an external field: The strong influence of tilted walls. *Phys. Rev. Lett.* **92**(185508), 1–4.

[32] WEITZ, L. R. & ZIMMER, E. J. (1984) Disclinations in a graphite fiber bundle. *Carbon* **22**, 209.

[33] WINCURE, B. & REY, D. A. (2006) Heterogeneous curved moving nematic–isotropic fronts. *J. Chem. Phys.* **124**(244902), 1–13.

[34] WINCURE, B. & REY, D. A. (2007) Computational modeling of nematic phase ordering by film and droplet growth over heterogeneous substrates. *Liq. Cryst.* **34**, 1397–1413.

[35] WINCURE, B. & REY, D. A. (2007) Growth and structure of nematic spherulites under shallow thermal quenches. *Contin. Mech. Thermodyn.* **19**, 37–58.

[36] WINCURE, B. & REY, D. A. (2007) Nanoscale analysis of defect shedding from liquid crystal interfaces. *Nano. Lett.* **7**, 1474–1479.

[37] YAN, J. & REY, D. A. (2002) Texture formation in carbonaceous mesophase fibers. *Phys. Rev.* **65**(031713), 1–14.